Accepted by ApJ - May 30, 2007
Preprint typeset using LaTeX style emulateapj v. 10/09/06

INFRARED SPECTRAL ENERGY DISTRIBUTIONS OF $Z \sim 0.7$ STAR-FORMING GALAXIES

X Z Z [1,2], H ´D [3], E F. B [1], E L F ' [4], G H. R [5], H -W R [1] D S [6]

Accepted by ApJ - May 30, 2007

ABSTRACT

We analyze the infrared (IR) spectral energy distributions (SEDs) for $10\mu\mathrm{m} < \lambda_{\rm rest} < 100\mu\mathrm{m}$ for ~ 600 galaxies at $z \sim 0.7$ in the extended Chandra Deep Field South by stacking their *Spitzer* 24, 70 and 160 μm images. We place interesting constraints on the average IR SED *shape* in two bins: the brightest 25% of $z \sim 0.7$ galaxies detected at 24 μm, and the remaining 75% of individually-detected galaxies. Galaxies without individual detections at 24 μm were not well-detected at 70 μm and 160 μm even through stacking. We find that the average IR SEDs of $z \sim 0.7$ star-forming galaxies fall within the diversity of $z \sim 0$ templates. While dust obscuration $L_{\rm IR}/L_{\rm UV}$ seems to be only a function of star formation rate (SFR; $\sim L_{\rm IR} + L_{\rm UV}$), not of redshift, the dust temperature of star-forming galaxies (with SFR $\sim 10\,\mathrm{M_\odot\,yr^{-1}}$) at a given IR luminosity was lower at $z \sim 0.7$ than today. We suggest an interpretation of this phenomenology in terms of dust geometry: intensely star-forming galaxies at $z \sim 0$ are typically interacting, and host dense centrally-concentrated bursts of star formation and warm dust temperatures. At $z \sim 0.7$, the bulk of intensely star-forming galaxies are relatively undisturbed spirals and irregulars, and we postulate that they have large amounts of widespread lower-density star formation, yielding lower dust temperatures for a given IR luminosity. We recommend what IR SEDs are most suitable for modeling intermediate redshift galaxies with different SFRs.

Subject headings: galaxies: evolution — galaxies: starburst — infrared: galaxies

1. INTRODUCTION

Dusty, intensely star-forming galaxies (SFR$> 10\,M_\odot\,\mathrm{yr^{-1}}$) are the dominant contributors to the $z \geq 0.5$ cosmic SFR density (e.g., Flores et al. 1999; Elbaz et al. 2002; Pozzi et al. 2004; Le Floc'h et al. 2005). The thermal dust emission from these galaxies accounts for much of the cosmic IR background, which contains half of the radiation energy of the extragalactic background light (Hauser & Dwek 2001; Lagache et al. 2005; Dole et al. 2006). Therefore understanding the IR SEDs of the dusty star-forming galaxies is essential for mapping the evolution of star formation as a function of cosmic time, and is a key observational ingredient of our understanding of galaxy evolution.

Detailed studies of the IR SEDs over the full range of 3-1000 μm have only been carried out for nearby galaxies (e.g., Dale et al. 2005), finding that the IR SED shape is correlated with dust temperature (Soifer & Neugebauer 1991; Dale & Helou 2002; Chapman et al. 2003; Lagache et al. 2003). Interestingly, despite this diversity of SED shapes, local galaxies' mid-IR (10-30 μm) luminosities are tightly correlated with their total IR luminosities with a scatter of ~ 0.3 dex (Chary & Elbaz 2001; Papovich & Bell 2002; Takeuchi et al. 2005b; Dale et al. 2005).

This *local* observation has often been used as a key assumption in studies exploiting deep mid-IR imaging from the *Infrared Space Observatory* at 15 μm and the *Spitzer Space Telescope* at 24 μm (e.g., Flores et al. 1999, 2004; Zheng et al. 2004; Hammer et al. 2005; Bell et al. 2005; Melbourne et al. 2005). Such studies have found significantly enhanced star formation at $0.5 \lesssim z \lesssim 1$, compared to the present day. Yet, this conclusion rests critically on the extent to which mid-IR luminosities reflect the total IR luminosity. Unfortunately, only a small fraction of mid-IR detected sources can be individually detected in the far-IR bands (e.g., *Spitzer* 70 & 160 μm), owing to limited signal-to-noise ratio (S/N) and source confusion (Dole et al. 2004b; Frayer et al. 2006). Thus, testing of this key assumption remains limited to the brightest sources (e.g., Sajina et al. 2006; Borys et al. 2006) or is indirect (e.g., Appleton et al. 2004; Yan et al. 2005; Pope et al. 2006; Marcillac et al. 2006).

The goal of this paper is to explore the average IR SEDs of a stellar mass-limited sample $z \sim 0.7$ galaxies in the extended Chandra Deep Field-South (E-CDFS). In previous works, we have shown that stacking noise-limited images of a set of galaxies allows one to securely detect the mean flux of the galaxy set substantially below the individual detection limit (Zheng et al. 2006; Dole et al. 2006). Here, we stack at longer wavelengths, i.e., 70 μm and 160 μm, to empirically determine the population-averaged IR SED. We combine these results with morphologies, and average fluxes at shorter wavelengths, to place constraints on the dust extinction and SEDs of these galaxies. In §2 we describe the multi-wavelength data used to construct galaxy SEDs and the samples of $z \sim 0.7$ galaxies. §3 presents our stacking methods. In particular we test the results of stacking noise and confusion limited 70 and 160 μm images. In §4 we present the properties of the average SEDs. Discussion and conclusion are given in §5. Throughout this paper, we assume $\Omega_M = 0.3$, $\Omega_\Lambda = 0.7$ and $H_0 = 70\,\mathrm{km\,s^{-1}\,Mpc^{-1}}$ for a Λ-CDM cosmology. All magnitudes are given in the Vega system except where otherwise specified.

2. THE DATA AND SAMPLES

2.1. *The data*

[1] Max-Planck Institut für Astronomie, Königstuhl 17, D-69117 Heidelberg, Germany
[2] Purple Mountain Observatory, Beijing-West Road 2, Nanjing 210008, P. R. China; xzzheng@pmo.ac.cn
[3] Institut d'Astrophysique Spatiale (IAS), bat 121, F-91405 Orsay (France); Université Paris-Sud 11 and CNRS (UMR 8617)
[4] Spitzer Fellow, Institute for Astronomy, University of Hawaii, 2680 Woodlawn Drive, Honolulu, HI 96822
[5] Steward Observatory, University of Arizona, 933 N Cherry Ave, Tucson, AZ 85721
[6] Department of Astronomy, Columbia University, New York, NY 100 27

We use *Spitzer* 24, 70 and 160 μm data to study the thermal dust emission of $z \sim 0.7$ galaxies. In addition, we include deep ultraviolet data from the *Galaxy Evolution Explorer* (GALEX: Martin et al. 2005a), optical data from the Classifying Objects by Medium-Band Observations (COMBO-17; Wolf et al. 2003) survey, and four band (3.6, 4.5, 5.8 and 8.0 μm) Infrared Array Camera (IRAC; Fazio et al. 2004) data to construct the stellar SED of a galaxy. These data cover wavelength range from 0.15 μm to 160 μm in the observed frame, equal to the rest-frame range ~0.09 to ~100 μm for $z = 0.7$.

The COMBO-17 survey has imaged the $30'.5 \times 30'$ E-CDFS in five broad (U, B, V, R and I) and 12 medium optical bands, providing high-quality astrometry (uncertainties $\sim 0''.1$) based on a very deep R-band image (26 mag at the 5σ limit), photometric redshifts ($\delta z/(1+z) \sim 0.02$ at $m_R < 23$; Wolf et al. 2004) and stellar masses (Borch et al. 2006) for $\sim 11,000$ galaxies with $m_R < 24$. We use the photometric redshift and stellar mass catalogs to select galaxy samples.

GALEX ultraviolet observations provided deep far-ultraviolet (FUV; 1350–1750Å) and near-ultraviolet (NUV; 1750–2800Å) images centered on the E-CDFS. The FUV and NUV images have a field of view of one square degree, a typical point-spread function (PSF) of full width at half-maximum (FWHM) $\sim 5''$, a resolution of $1''.5$ pixel^{-1} and a depth of 3.63 μJy at the 5σ level. The data reduction and source detection is described in Morrissey et al. (2005).

The deep IRAC 3.6, 4.5, 5.8 and 8.0 μm imaging data and MIPS 24, 70 and 160 μm imaging data were obtained as part of the first run of MIPS GTO observations (Rieke et al. 2004). A rectangular field of $\sim 90' \times 30'$ was observed in all bands (with small shifts between different bands). The effective exposure time is 500 s for the four IRAC band images, 1378 s pix^{-1} for MIPS 24 μm, 600 s pix^{-1} for 70 μm and 120 s pix^{-1} for 160 μm. IRAC 3.6 and 4.5 μm images have a PSF of FWHM $\sim 1''.8$ and 5.8 and 8.0 μm images have a PSF of FWHM $\sim 2''.0$ (Huang et al. 2004). The 24 μm image has a PSF of FWHM $\simeq 6''$. Sources are detected at 24 μm down to 83 μJy (at 80% completeness; see Papovich et al. 2004 for details of data reduction, source detection and photometry). The 70 μm image is characterized by a PSF of FWHM $\simeq 18''$ and a resolution of $9''.9$ pixel^{-1}. The 160 μm image has a PSF of FWHM $\simeq 40''$ and a resolution of $16''$ pixel^{-1}. Sources with fluxes of $f_{70} > 15$ mJy can be individually resolved at 70 μm and of $f_{160} > 50$ mJy at 160 μm (see Dole et al. 2004a, for details).

We take COMBO-17 astrometry as the reference coordinate and cross-correlate all other band catalogs with the COMBO-17 catalog. In each cross-correlation, we use bright stars and compact sources to estimate the systematic offsets and uncertainties between two coordinates. A position tolerance of 4σ uncertainty is adopted so that objects in the two catalogs having coincident coordinates within the tolerance (corrected for the systematic offsets) are identified as the same objects. The nearest COMBO-17 object is chosen if multiple ones exist within the tolerance. The adopted tolerances are $2''.5$ (FUV), $3''.0$ (NUV), $1''.0$ (3.6 μm), $1''.2$ (4.5 μm), $1''.5$ (5.8 and 8.0 μm) and $2''.2$ (24 μm). For the 70 and 160 μm catalogs, we firstly cross-correlate them with the 24 μm catalog as individually-detected 70 and 160 μm sources are bright at 24 μm; we then associate 70 and 160 μm objects with COMBO-17 objects using the coordinates of the corresponding 24 μm sources. The tolerance between 70/160 and 24 μm is $5''/16''$ respectively.

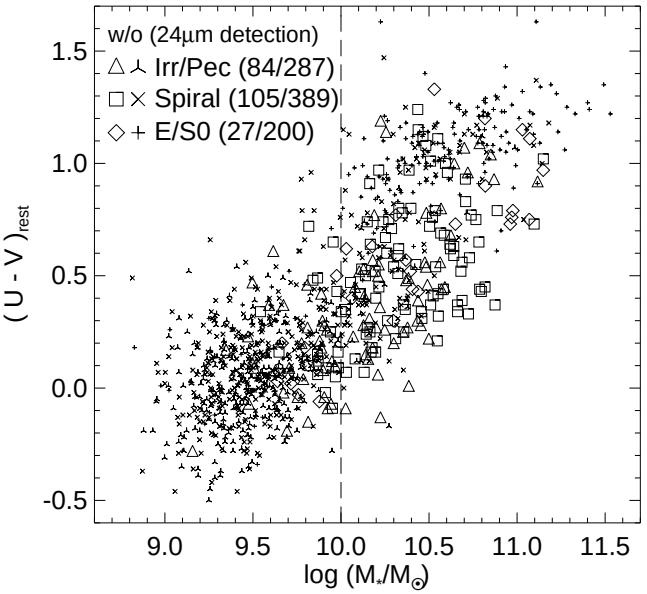

F . 1.— The rest-frame color $U - V$ versus stellar mass for a sample of 1092 galaxies of known (GEMS) morphology in the redshift slice $z = 0.7 \pm 0.05$. Open symbols show the objects detected individually at 24 μm ($f_{24} > 83\mu$Jy) and skeletal symbols represent individually-undetected ones. Most red ($U - V$ >0.7) elliptical/lenticular galaxies and blue ($U - V$ <0.7) small (M_* <10 $M_\odot$) spiral/irregular/peculiar galaxies are not individually detected at 24 μm. The number of objects in each category is given in the brackets. The *dashed* line shows the mass cut $M_* = 10^{10} M_\odot$ that we apply in the subsequent analysis.

2.2. *The samples*

We combine spectroscopic redshifts from the VLT VIMOS Deep Survey (Le Fèvre et al. 2005) and the GOODS survey (Vanzella et al. 2005, 2006) with photometric redshifts from the COMBO-17 survey (Wolf et al. 2004) to select sample galaxies. The E-CDFS has HST imaging from the Galaxy Evolution from Morphology and SEDs (Rix et al. 2004, GEMS;) Survey. Visually classified morphologies are available for 1458 galaxies with $m_R < 24$ in a thin redshift slice $z = 0.7 \pm 0.05$ (Bell et al. 2005). Of the 1458 galaxies, 1114 galaxies have all observations, including GALEX, IRAC and MIPS observations. To avoid contamination from active galactic nuclei (AGNs), we remove 22 X-ray detected sources in the Chandra 250 ks observation (Lehmer et al. 2005), leaving a sample of 1092 galaxies. Spectroscopic redshifts are available for 64% of the sample galaxies. The contribution from the X-ray-undetected AGNs to the total 24 μm luminosity of $z < 1$ galaxies is suggested to be <~ 10% (Zheng et al. 2006; Brand et al. 2006). This will not have significant effects on our results.

The sample demographics are shown in Figure 1. The sample is limited by R-band apparent magnitude ($m_R < 24$), corresponding to approximately the rest-frame B-band at $z \sim 0.7$. Accordingly, the completeness of the sample, in terms of stellar mass, is a strong function of color: the mass limit for red (old or dusty) galaxies is $M_* \sim 10^{10} M_\odot$ whereas blue galaxies can be included down to almost $M_* \sim 10^9 M_\odot$. We choose to impose a stellar mass cut of $M_* \geq 10^{10} M_\odot$ in what follows; not only are almost all 24 μm emitters above this mass cut, but also the completeness of this sample is not a strong function of color (i.e., age or dust obscuration). We also select another sample to explore the relationship between the IR SED shape and 24 μm luminosity; we extend the redshift slice to 0.6< z <0.8 to increase the number of sample galax-

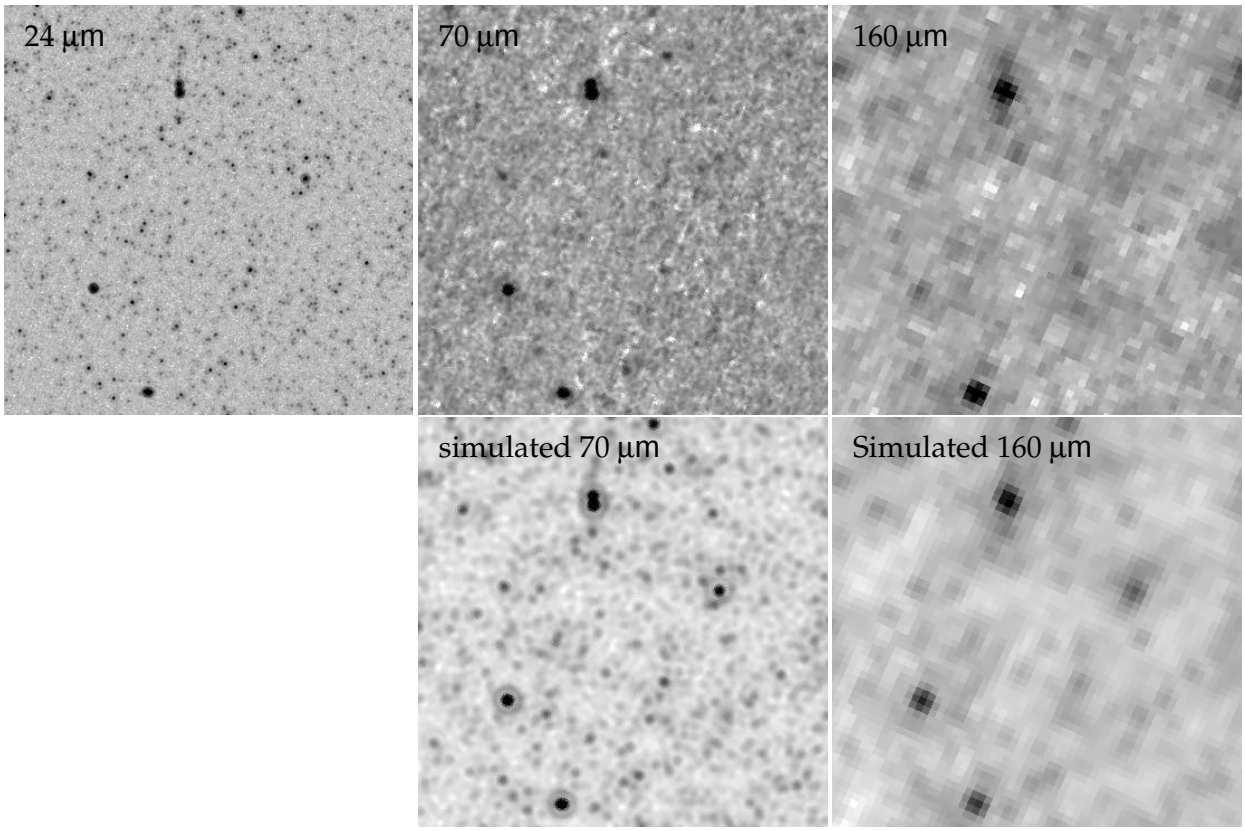

F . 2.— Observed MIPS 24, 70 and 160 μm image sections ($15' \times 15'$) in the extended CDFS and simulated 70 and 160 μm images. The simulated 70 and 160 μm images are created by degrading the 24 μm image to the 70 and 160 μm resolution. No additional noise is added to the simulated images.

ies. The final sample then comprises some 579 galaxies with $M_* \geq 10^{10}\,M_\odot$ in the redshift range $0.6< z <0.8$. Of them, 218 are individually-detected at 24 μm with fluxes in excess of $> 83\mu$Jy; none is individually detected at 70 or 160 μm. X-ray detected sources have been excluded.

3. IMAGE STACKING

As outlined earlier, current missions are unable to yield individual detections for the vast majority of intermediate-redshift objects at far-IR wavelengths, owing both to contributions from instrumental noise and confusion noise. In order to place constraints on the shape of the IR SEDs of 'typical' star-forming intermediate redshift galaxies, stacking on the positions of known star-forming galaxies can lower the effective noise (Zheng et al. 2006), allowing detection of the 'average' galaxy. In Zheng et al. (2006) we presented a description of stacking of 24 μm data (in that case to resolve the 24 μm luminosity of dwarf galaxies); we briefly summarize the most important aspects of 24 μm stacking in §3.1. The focus of this paper is stacking at longer wavelengths, at 70 μm (PSF FWHM 18″) and 160 μm (FWHM 40″), discussed in §3.2.

3.1. *FUV, NUV and MIPS 24 μm image stacking*

While much of this paper describes stacking results for subsamples that are individually detected at 24 μm, some subsamples are not individually detected at 24 μm. Furthermore, the 24 μm, FUV and NUV images share many of the same characteristics: the PSFs have similar FWHM, and at each wavelength, $\gtrsim 1/2$ of the extragalactic background at that wavelength is resolved by these images (i.e., the images are only mildly confusion-limited; e.g., Papovich et al. 2004; Xu et al. 2005; Dole et al. 2006). Accordingly, stacking of FUV, NUV and 24 μm images is carried out in the same way (see Zheng et al. 2006, for more details).

Three basic steps are adopted to derive the mean fluxes for galaxy subsets. First, we subtract all individually-detected sources from the images. This is done using the software tool STARFINDER[7] (Diolaiti et al. 2000) with an empirical PSF constructed from 18/42/56 bright point sources at 24 μm/FUV/NUV respectively. Then we perform mean stack of the residual image postage stamps centered on the optical coordinates of the objects that are individually undetected in the subset of interest. An aperture of 5″ is used to integrate the central flux of the mean-stacked image and estimate the background from the outer regions. Aperture corrections of a factor of 1.88/1.19/1.14, derived from the empirical PSF at 24 μm/FUV/NUV respectively, are adopted to calibrate the stacked fluxes to the total fluxes. Last we sum the fluxes of individually-detected sources and the stack flux of individually-undetected sources in each galaxy subset, giving the mean 24 μm/FUV/NUV fluxes. Uncertainties are derived from bootstrapping.

3.2. *MIPS 70 and 160 μm image stacking*

The 70 μm and 160 μm PSFs are considerably larger than those at shorter wavelengths, yielding confused images, resolving only the brightest, relatively nearby sources — some <30% of the extragalactic background at this wavelength (Dole et al. 2004a). Galaxies at $0.6 < z < 0.8$ are heavily confused in all but the brightest cases (Dole et al. 2004a; Lagache et al. 2003, 2004), requiring stacking to gain insight

[7] STARFINDER gives identical results within the errors to the tool ALLSTAR in IRAF package.

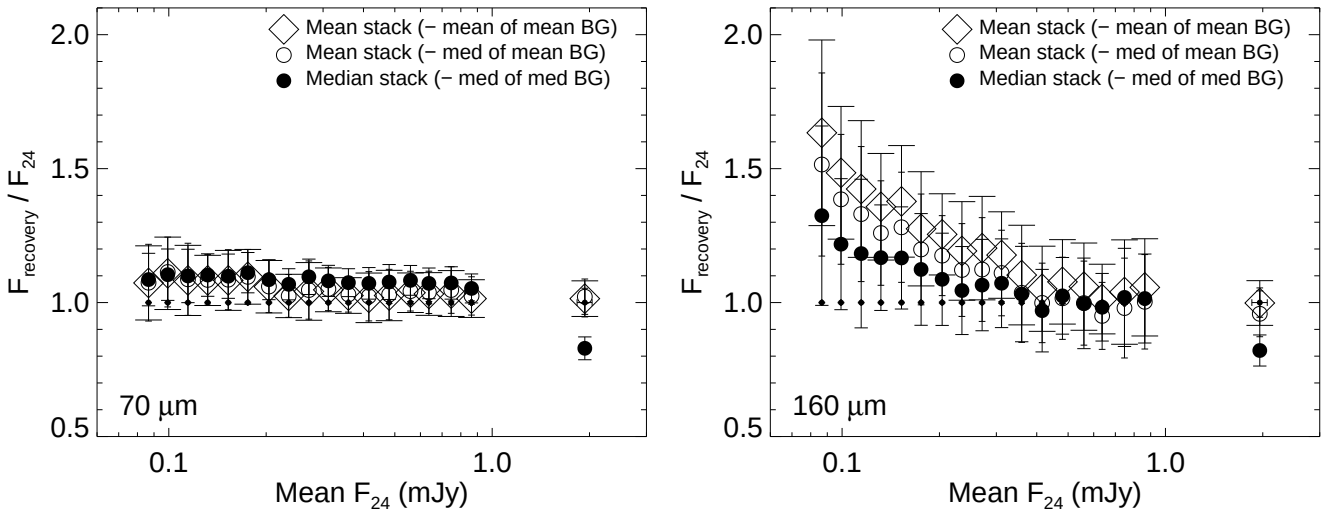

F . 3.— Recovery of the mean fluxes of *randomly* distributed 24 μm sources through stacking after convolution to the 70 μm (*left*) and 160 μm (*right*) resolution. The fluxes were taken from the 8255 individually-resolved sources in the $\sim 1.^{\circ}5 \times 0.^{\circ}5$ 24 μm image and were split into 18 flux bins in the range from 83 μJy to 10 mJy. The number of objects in each bin decreases with increasing flux. Three measures of the stack flux are presented for each bin: the integrated central flux of the *mean* stack using the *mean* background for sky subtraction; the integrated central flux of the *mean* stack using the *median* background; and the integrated central flux of the *median* stack using the *median* of the background (see text for details). Errorbars are derived from bootstrapping. While the flux can be recovered with little bias at 70 μm resolution, flux recovery at 160 μm leads to a systematic overestimate.

TABLE 1
T 18 8255 - 24 μ .

No.	1	2	3	4	5	6	7	8	9	10	11	12	13	14	15	16	17	18
$< f_{24} >$(μJy)	87	99	115	132	153	176	204	235	271	311	359	416	480	559	637	747	863	1946
Number	1070	1259	1067	894	803	683	508	418	328	267	222	174	134	98	72	46	39	169

into their long-wavelength IR SEDs (see, e.g., Dole et al. 2006).

The large angular extent of the long-wavelength PSFs poses a significant challenge for those wishing to estimate their average properties. At $z = 0.7$, the PSF size of the 70 μm image (FWHM $\simeq 18''$) corresponds to a physical scale of $\sim$130 kpc. For the 160 μm image (PSF FWHM $\simeq 40''$), the corresponding scale is $\sim$290 kpc. Thus, the stacking results are a reflection of the IR-luminosity weighted two-point correlation function on $\gtrsim 100$ kpc scales, overestimating the true average fluxes of the galaxies of interest.

In order to understand this source of systematic error in better detail, we carried out some simulations where synthetic 24 μm data (using the observed positions and fluxes of individually-detected 24 μm sources) are degraded in resolution to the resolution of the 70 μm and 160 μm data. For the purposes of this test, we assume a constant ratio between 24 μm flux and the wavelength of interest. We explore two cases. First, the positions are randomly scrambled (i.e., the relative brightnesses of galaxies are preserved but their positions are random). This test gives an indication of the systematic effects of stacking randomly-positioned sources. The second case is when both the fluxes and positions of sources are preserved. This second case is our 'best' estimate of the likely systematic uncertainties of stacking in a realistically-clustered case. Figure 2 shows the 24 μm images degraded to the 70 and 160 μm resolution respectively, compared with the observed MIPS 24, 70 and 160 μm images. Because of confusion, only a handful of bright 24 μm sources can be individually resolved in the degraded images. Through stacking the mean flux can be estimated for 24 μm source subsets; the accuracy of the recovery of the mean flux shows how well stacking works at that corresponding image resolution.

3.2.1. *Stacking randomly distributed sources*

The whole 24 μm mosaic image of the E-CDFS covers a rectangular sky area of $\sim 1.^{\circ}5 \times 0.^{\circ}5$ and contains 8255 individually-detected sources at 5σ detection limit (83 μJy). The vast majority of the 8255 sources ($f_{24} > 83\mu$Jy) are point sources. Replacing all sources with the 24 μm PSF (empirically constructed from bright stars), we generated an artificial 24 μm image having the 8255 sources *randomly* distributed into a $\sim 1.^{\circ}5 \times 0.^{\circ}5$ blank field. The artificial 24 μm image was then degraded to the 70 and 160 μm image resolution respectively. The degraded images are then stacked at the 24 μm source positions, giving indications as to the expected quality of stacking results at 70 μm and 160 μm. We note that the replacement of the background blank field with the PSF-subtracted 24 μm image (having some contribution from individually-undetected sources) does not modify our results significantly in the mean, adding only some modest additional scatter.

The 24 μm sources were sorted into 18 bins in flux, ranging from 83 μJy to 10 mJy (see also Dole et al. 2006), with $\sim$ 1000 objects per bin at faint flux levels, and $\lesssim 100$ per bin at brighter fluxes. The numbers of sources and average 24 μm fluxes per bin are listed in Table 1. In real stacks, we choose to PSF-subtract out the individually-detected sources, stacking the remaining image (in order to reduce bias from bright sources in background estimates). In the real 70 and 160 μm images, we detect $\sim$ 130 sources in each image. Thus, we must subtract approximately this many bright sources from

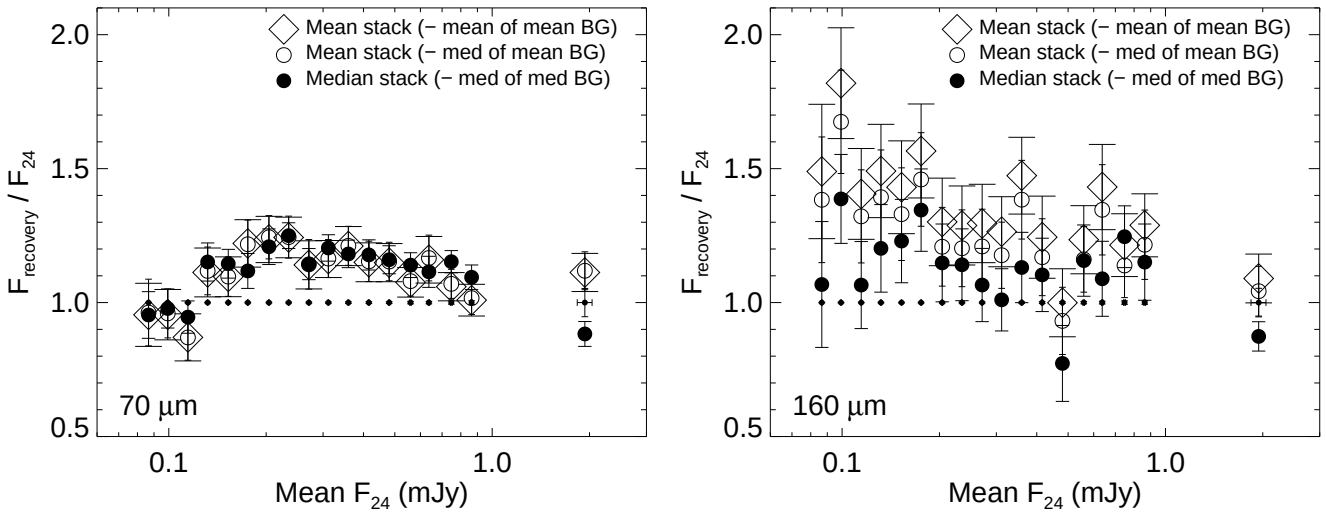

F . 4.— The recovery of the mean properties of 24 μm-detected sources at their observed positions. *Left*: Stacking results at 70 μm resolution. *Right*: Stacking results at 160 μm resolution. The errorbars reflect the variance from bootstrapping.

the simulated images before stacking to avoid unrealistically biasing the results. Ideally, one would subtract all detected sources in the simulated 70 and 160 μm images; unfortunately, as the simulated and real 70 and 160 μm images have (unavoidably) somewhat different noise and brightness distribution properties, the number of detected sources is different, and substantially higher in the case of (the rather deeper) simulated 70 μm data. Thus, we choose to PSF-subtract the 169 brightest sources (the brightest of the 18 original bins) before stacking for the remaining 17 bins.

For each flux bin, postage stamps were cut from the simulated image centered on the positions of the sources and were stacked. The size of postage stamps is 2.′5×2.′5 for the 70 μm image and $4' \times 4'$ for the 160 μm image, allowing for a proper background estimate. Two stacked images were created for each bin through averaging or medianing. For the stacked 70 μm postage stamp images, an aperture of radius 0.′49 is used to integrate the central stack flux and an annulus with inner radius 0.′82 and outer radius 1.′23 to estimate the background. For the stacked 160 μm postage stamp images, the corresponding aperture is of radius 1.′07 and the corresponding annulus is of inner radius 1.′07 and outer radius 1.′87. The mean and median of pixels in the annulus region were taken as the background of the mean-stacked image for sky subtraction. Only the median (nearly identical to the mean) was adopted as the background of the median-stacked image. Therefore, we derive three measures of the stack flux for each subsample: the integrated central flux of the *mean* stack using the *mean* background for sky subtraction; the integrated central flux of the *mean* stack using the *median* background; and the integrated central flux of the *median* stack using the *median* of the background. Finally, aperture corrections derived from model PSFs (http://ssc.spitzer.caltech.edu/mips/psffits/) were applied to correct the estimates of stack flux to the total. The aperture correction is a factor of 1.30 for 70 μm, 1.25 for 160 μm using the median background, and 1.34 for 160 μm using the mean background.

Figure 3 shows the results of stacking *randomly* distributed sources at 70 and 160 μm resolution. Uncertainties are derived from bootstrapping. At 70 μm resolution, the mean flux of 24 μm sources of comparable flux can be properly recovered over a flux range of one order of magnitude. At 160 μm resolution, recovered fluxes are of reasonable quality at bright limits, and become progressively more biased (by ~ 20-50%) towards fainter limits. After some investigation, it became clear that the the stack recovery at 160 μm is correlated with the number of objects in the stack bin. The increase of objects in number leads to an increase of the overlap between these objects within a fixed area. This increasing overlap leads to an increase of the stack flux relative to the input flux. By stacking a number of identical sources without background and foreground sources, we obtained similar results as shown in Figure 3. Indeed a point source contains 80% of its flux in an area of 3.6 arcmin^2 in the 160 μm imaging and an area of 0.9 arcmin^2 in the 70 μm imaging. To fill in a $1.^\circ5 \times 0.^\circ5$ field, it requires around 750 160 μm sources or 3000 70 μm sources, compared to ~ 50 - 1260 objects in the stack bins. Therefore the stack results at 70 μm are little affected by the overlap between the stack objects but the stack results at 160 μm are significantly influenced for stack bins of ~ 1000 objects.

The three measures of the stack flux are nearly identical within the errorbars (~ 10%) for simulated 70 μm stacking and slightly different for simulated 160 μm stacking, in particular for the low flux bins, although the scatter is significant (~ 10 - 25%). Note that we divided sources into stack bins in terms of their fluxes. For the stack bins having sources whose fluxes span a wide range, the median stack substantially underestimates the mean flux.

3.2.2. *Stacking sources at their observed positions*

In order to build a more realistic picture of the expected uncertainties from stacking at 70 μm and 160 μm, we repeat the last analysis except we keep both the fluxes and positions of the sources fixed to those observed at 24 μm. This gives insight into the influence of clustering on the results. In this test, the observed 24 μm map was degraded to the 70 and 160 μm resolution respectively, as shown in Figure 2. As previously, sources were split into 18 bins in 24 μm flux, and the stacking results for each flux bin were calculated. Figure 4 shows the results. Comparing the results with Figure 3, one can clearly see that the mean and median recovered fluxes are significantly affected by the clustering of sources on the sky. In general, our test suggests that stacking subsets of 70 μm and 160 μm sources may overestimate the mean flux somewhat;

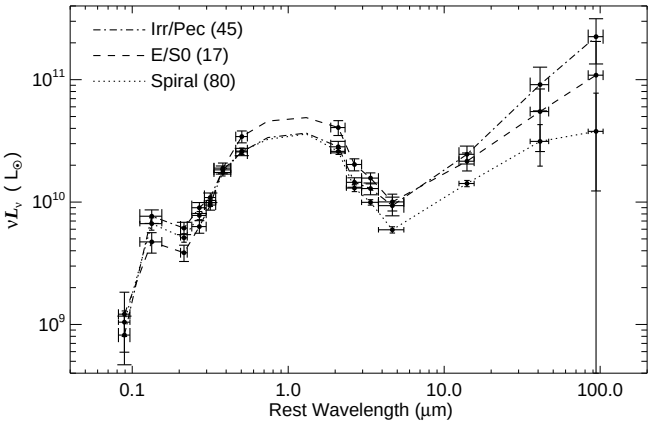

F . 5.— The average SED, spanning a factor of 1000 in wavelength, as a function of morphological type for 24 μm detected ($f_{24} > 83\mu$Jy) galaxies with $M_* \geq 10^{10}\,M_\odot$ in a thin redshift slice $0.65 \leq z \leq 0.75$. Vertical errorbars are the 1σ uncertainties derived from bootstrapping and horizonal errorbars show the band widths. The number of objects in each morphology bin is given in the brackets.

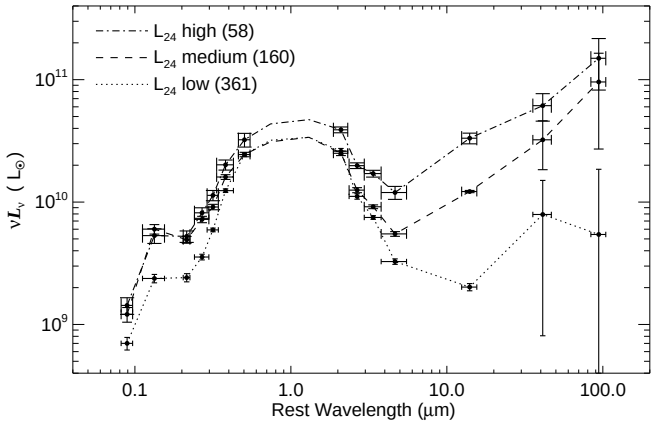

F . 6.— Average SED as a function the 24 μm luminosity for galaxies with $M^* \geq 10^{10}\,M_\odot$ in the redshift range $0.6 < z < 0.8$. The vertical errorbars show the 1σ uncertainties and horizonal errorbars show the band widths. The 579 galaxies are split into three bins in terms of their 24 μm luminosities: L_{24}-high, L_{24}-medium and L_{24}-low. The numbers in brackets denote the number of objects included in each bin.

typical biases are ~ 20%, with uncertainties of order ~ 20%. Yet, the magnitude and direction of these effects on different subsamples are difficult to estimate *a priori*. Figure 4 demonstrates that from bin to bin, the source clustering may lead to either an increase or a decrease of the mean flux of the source subsample, depending on the actual distribution and density of sources of different brightnesses on the sky.

3.2.3. *Stacking $z \sim 0.7$ galaxies*

The above tests demonstrate that it will be difficult to estimate the mean flux at 70 μm and 160 μm to better than ~ 20%, and that the extent of the bias towards higher or lower flux is difficult to predict with accuracy. In this paper, we adopt a pragmatic approach: for each subsample that is stacked at 70 μm and 160 μm, we attempt to derive an individual 'bias correction' based on the 24 μm image. Sources bright at 24 μm are generally bright at 70 and 160 μm, although the 24 μm to 70 or 160 μm flux ratio varies from object to object at a scatter at the 0.5 dex level (Dale et al. 2005). Thus, we adopt the simplistic assumption that the 24 μm image can be taken as a good proxy for the 70 or 160 μm image at $\simeq 6''$ resolution and high S/N; 70 μm and 160 μm resolution images derived under this assumption (Fig. 2) appear a reasonable description of the real 70 μm and 160 μm images. Thus, for a given subset of $z \sim 0.7$ galaxies, we estimated precisely the mean 24 μm flux from their 24 μm images. Then we degraded the 24 μm images to 70 and 160 μm image resolution. Two stack fluxes were estimated by stacking each of the two sets of degraded images. By comparing the stack fluxes to the actual mean 24 μm flux of the galaxy subset, we obtained empirical corrections, which were applied to the corresponding 70 and 160 μm stack fluxes of the subset of $z \sim 0.7$ galaxies, respectively. Uncertainties in this correction are applied also, in quadrature, to the derived stacking results at 70 μm and 160 μm.

4. RESULTS

To explore the average IR SEDs of $z \sim 0.7$ star-forming galaxies, we first look into the dependence of the IR SED shape on galaxy morphology. Then, we investigate the relationship between the IR SED shape and the 24 μm luminosity and the $z \sim 0.7$ IR SEDs to those of present-day star-forming galaxies. Finally, based on the IR SEDs, the extrapolation of the total IR luminosity from the 24 μm luminosity is discussed.

4.1. *The relationship between IR SED and morphology*

We used a sample of 1092 galaxies of known morphology to investigate the dependence of the IR SED shape on morphology. The 1092 galaxies are classified into three morphological types: elliptical/lenticular (E/S0), spiral, and irregular/peculiar. Figure 1 shows the relationship between the rest-frame color $U - V$ and stellar mass. Objects detected at 24 μm ($f_{24} > 83\mu$Jy) are marked with open symbols and undetected ones with skeletal symbols. The detection limit of 83 μJy corresponds to the monochromatic observed-frame 24 μm luminosity $\nu L_{\nu,24} = 6 \times 10^{10}\,L_\odot$ at $z = 0.7$. The 24 μm-undetected galaxies are intrinsically faint in the IR bands (see §4.2), and we excluded them in constructing these composite SEDs. To avoid selection bias in color (see §2.2), we also excluded about one third of the 24 μm detected galaxies with $M_* < 10^{10}\,M_\odot$, leaving 152 galaxies in the final sample. We calculated the average luminosities in 14 bands for each subsample of 24 μm-detected galaxies: FUV & NUV from GALEX, U, B, V, R and I from the COMBO-17 survey, IRAC 3.6, 4.5, 5.8 and 8.0 μm, MIPS 24, 70 and 160 μm bands. The average luminosity of each band includes contributions from both individually-detected and individually-undetected sources (at wavelengths other than 24 μm). Errors in the average luminosities were derived from bootstrapping, including contributions to the uncertainty from measurement errors in both the individually-detected fluxes and the individually-undetected fluxes. The average SED spans a range in the rest-frame of 0.1 to 100 μm.

Figure 5 shows the average SEDs of the three subsamples. Each of the three average SEDs is dominated by a dust-extincted stellar spectrum at $\lambda < 5\,\mu$m and emission by dust at $\lambda > 5\,\mu$m. Irregular/peculiar galaxies show a higher ratio of dust to stellar emission compared to the spirals and E/S0 galaxies. The slope of the IR SED (rest-frame 10-100 μm) is steeper for irregular/peculiar galaxies, somewhat intermediate for E/S0 galaxies, and lowest for spirals although the uncertainties of 70 and 160 μm luminosities are large. The irregular/peculiar galaxies usually form stars in relatively concentrated regions, leading to a high star formation intensity (i.e. SFR per unit area). In contrast, the spirals are often char-

TABLE 2
A - $0.6 < z < 0.8$.

N_{obj}	$\log < M^* >$ ($M_\odot$)	$\log \nu L_{\nu,24}$ ($L_\odot$)	$\log \nu L^a_{\nu,70}$ ($L_\odot$)	corr.(70)	$\log \nu L^a_{\nu,160}$ ($L_\odot$)	corr.(160)	$\log < L_{12--100} >^b$ ($L_\odot$)	$\log < L_{IR} >^c$ ($L_\odot$)
58	10.7	$10.52^{+0.04}_{-0.05}$	$10.79^{+0.10}_{-0.13}$	1.51±0.24	$11.17^{+0.16}_{-0.26}$	1.04±0.39	$11.30^{+0.10}_{-0.13}$	$11.42^{+0.07}_{-0.08}$
160	10.5	$10.09^{+0.01}_{-0.01}$	$10.51^{+0.16}_{-0.24}$	1.03±0.32	$10.98^{+0.23}_{-0.55}$	0.92±0.61	$11.04^{+0.16}_{-0.27}$	$11.12^{+0.05}_{-0.05}$
361	10.7	$9.31^{+0.03}_{-0.03}$	$9.90^{+0.28}_{-0.99}$	1.19±0.96	<10.27	...	$10.18^{+0.26}_{-0.75}$	$10.28^{+0.14}_{-0.21}$

[a] The 70 μm and 160 μm luminosities estimated from stacking have included the corrections derived from degraded 24 μm images. The corrections are listed in the table.[b] $L_{12--100}$ is the luminosity between 12 to 100 μm, calculated by linearly interpolating observed 24, 70 and 160 μm luminosities (in logarithm space).[c] L_{IR} refers to the total IR luminosity between 8 to 1000 μm. Local IR SED templates from Lagache et al. (2004),Chary & Elbaz (2001) and Dale & Helou (2002) are used to fit the observed data points. The total IR luminosity is derived from the dust temperature-match templates. See text for details.

acterized by a relatively low star formation intensity as the star-forming regions are widely distributed over disks. The star formation density for the E/S0 galaxies is somewhat between those of the irregular/peculiar galaxies and spirals. The shapes of the IR SEDs are thus a function of star formation intensity in the sense that the dust temperature is primarily colder in systems of relatively lower star formation intensity (we will return this topic in §5).

4.2. *The relationship between IR SED and 24 μm luminosity*

We used a mass-limited sample to study the relationship between IR SED shape and 24 μm luminosity. This sample consists of 579 galaxies with $M^* \geq 10^{10}\,M_\odot$ and $0.6 < z < 0.8$. The sample galaxies were divided into three 24 μm luminosity bins: L_{24}-high, L_{24}-medium and L_{24}-low. The first two bins contain 218 individually-detected 24 μm sources (f_{24} >83 μJy) and all individually-undetected 24 μm sources (361 of the 579) are in the third bin. The L_{24}-high bin is chosen to contain 58 brightest 24 μm sources so that its total 24 μm luminosity equals that of the L_{24}-medium bin. Consequently the stacked 70 and 160 μm fluxes are expected to have comparable signal-to-noise ratios for the two bins. Average luminosities in all 14 bands were calculated for the three subsets of galaxies. The average luminosities in the 24, 70 and 160 μm bands are listed in Table 2, along with the number of objects and mean stellar mass for each of the three subsets. The empirical corrections adopted for the 70 and 160 μm stack fluxes (see §3.2.3) are also presented. Errors include the uncertainties in measurements and bootstrapping errors. Figure 6 shows the average SED from the rest-frame wavelengths 0.1 to 100 μm as a a function of the 24 μm luminosity. It is clear that the observed 24 μm (rest-frame 14 μm) luminosity is correlated with the 70 and 160 μm IR luminosities for massive galaxies at $z \sim 0.7$ in the sense that the 70 and 160 μm IR luminosities increase as the 24 μm luminosity increases; i.e., 24 μm luminosity typically reflects high IR luminosity, rather than an enhanced rest-frame mid-IR excess (see also Bavouzet et al. 2007, in preperation). The L_{24}-high bin has an average galaxy stellar mass 0.2 dex larger than the L_{24}-medium bin; this can also be seen from the redder optical colors and higher rest-frame ~ 3 μm luminosity of the L_{24}-high bin. The L_{24}-low bin contains 361 massive galaxies that are individually undetected at 24 μm, including early-type galaxies with little star formation and late-type galaxies in the quiescent star formation phase (see Figure 1). The short-wavelength part of their average SED is dominated by a relatively old stellar population. The large errorbars of the 70 and 160 μm luminosities compared to the small errorbar of the 24 μm luminosity are partially due to the intrinsic scatter among the sample galaxies in this bin.

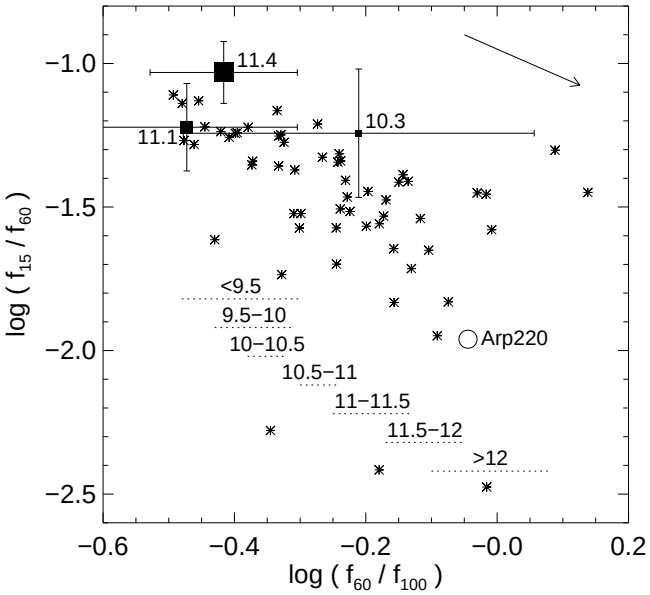

F . 7.— Relative dust temperature estimate from the IR flux ratio f_{60}/f_{100} versus f_{15}/f_{60}. *Asterisks* represent local star-forming galaxies from Dale et al. (2000) with IRAS observations at the 60 and 100 μm and ISO observation at 15 μm. The ratio f_{60}/f_{100} is an indicator of the dust temperature, which tends to be correlated with IR luminosity in the local Universe. The *dotted lines* show typical values of f_{60}/f_{100} corresponding the given $\log(L_{IR}/L_\odot)$ derived from IRAS data (Soifer & Neugebauer 1991). These lines are arbitrarily positioned on the Y-axis. The *open circle* shows the well-known local ultraluminous IR galaxy Arp 220. The *squares* show the three subsets of massive ($M^* \geq 10^{10}\,M_\odot$) galaxies in redshift slice $0.6 < z < 0.8$, labeled with the corresponding IR luminosities $\log(L_{IR}/L_\odot)$. Note that errorbars of the two flux ratios are not independent. The arrow indicates the effect of an increase in f_{60} by a factor of 1.5.

4.3. *Comparison with local SEDs*

A key goal of this paper is to compare the observed average IR SED shapes at $z \sim 0.7$ to local 'template' SEDs. We adopted a sample of local star-forming galaxies from Dale et al. (2000) with *IRAS* and ISO 15 μm observations and total IR luminosity (8 - 1000 μm) spanning from ~ 10^9 to $10^{12}\,L_\odot$. Figure 7 shows these nearby galaxies in the IR flux ratio f_{60}/f_{100} versus f_{15}/f_{60} plot. The local galaxies distribute along a sequence with considerable scatter. The sequence is correlated with both dust temperature and IR luminosity. The dust temperature and IR luminosity increase for increasing f_{60}/f_{100} (e.g., Soifer & Neugebauer 1991). The average IR SEDs for $z \sim 0.7$ galaxies are determined by the three MIPS bands, corresponding to the rest-frame ~14, ~41 and ~94 μm bands. The 24 μm and 160 μm luminosities can be

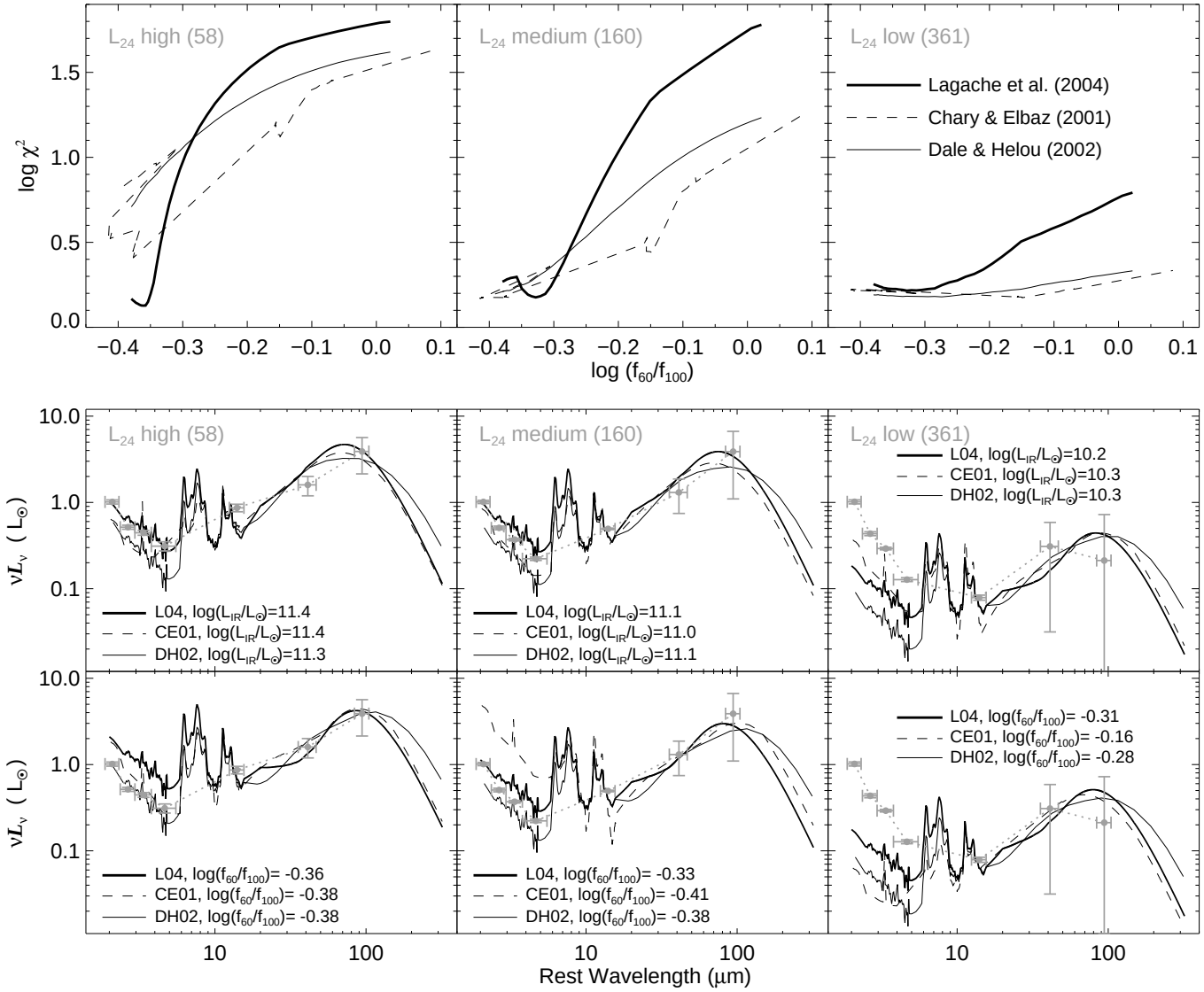

F . 8.— Fitting three sets of local templates from Lagache et al. (2004), Chary & Elbaz (2001) and Dale & Helou (2002) to the average IR SEDs of three subsets of massive ($M^* \geq 10^{10}\,M_\odot$) galaxies in the redshift slice $0.6< z <0.8$. Only the three MIPS data points (24, 70 and 160 μm) of each observed IR SED are used in the fitting. *Top*: The panels show χ^2 as a function of the template's characteristic $\log(f_{60}/f_{100})$. For each observed IR SED two best-fit templates are chosen: one is matched in luminosity (i.e., with the normalization constant equal to unity) and the other is dust temperature match (or SED shape match; i.e., with the minimum χ^2). *Bottom*: The *upper panels* shows the best-fit luminosity match templates and the *lower panels* show the best-fit dust temperature match templates, compared to the observed SEDs from the rest-frame 2 to 100 μm delineated by IRAC and MIPS data points for the L_{24}-high bin (*left panels*), the L_{24}-medium bin (*middle panels*) and the L_{24}-low bin (*right panels*). The SEDs are normalized to unity at 2.1 μm. Note that the stellar components of the locoal templates are somewhat arbitrarily set. The disagreements between the averaged SEDs and the best-fit templates at $\lambda_{\rm rest} < 5\mu$m should be ignored.

taken as rest-frame 15 μm and 100 μm luminosities, for which '*K*-corrections' are negligible. We estimated the rest-frame 60 μm luminosity by linear interpolation between the MIPS measurements in log-log space (as shown in Figure 6). We used the local sample to test the linear interpolation. First, we derive the 41 μm fluxes by linear interpolation between *IRAS* 25 and 60 μm measurements in log-log space. Second, we derive 60 μm fluxes by the same method between 41 and 100 μm for the 59 local galaxies adopted. The estimated 60 μm fluxes are 25±11% lower than the observed *IRAS* 60 μm fluxes. This hints that our rest-frame 60 μm luminosities of the $z \sim 0.7$ galaxies might be underestimated. We compared the $z \sim 0.7$ galaxies to the local galaxies. As shown in Figure 7, the two populations are roughly located in the same region of the f_{60}/f_{100} versus f_{15}/f_{60} plane. Specifically, the $z \sim 0.7$ star-forming galaxies of IR luminosity $11 < \log(L_{\rm IR}/L_\odot) < 11.4$ (those in the L_{24}-high bin and L_{24}-medium bin; the estimates of the total IR luminosities will be discussed later) populate the relatively low-temperature end of the template sequence. In the local Universe, these low-temperature galaxies tend to be of relatively low luminosity $\log(L_{\rm IR}/L_\odot) < 10.5$. This, with significant uncertainties, suggests that the typical dust temperature of $z \sim 0.7$ luminous IR galaxies (LIRGs; i.e., galaxies with $\log(L_{\rm IR}/L_\odot) > 11$) is lower than that of local galaxies of comparable IR luminosity. The IR flux ratios are poorly determined for the L_{24}-low bin because of the large uncertainties in the average 70 and 160 μm IR luminosities, which are partially due to the intrinsic scatter among the sample galaxies in the L_{24}-low bin (including early-type galaxies and late-type galaxies in the quiescent star formation phase).

We compared our average SEDs with the IR SED model templates from Lagache et al. (2004), Chary & Elbaz (2001)

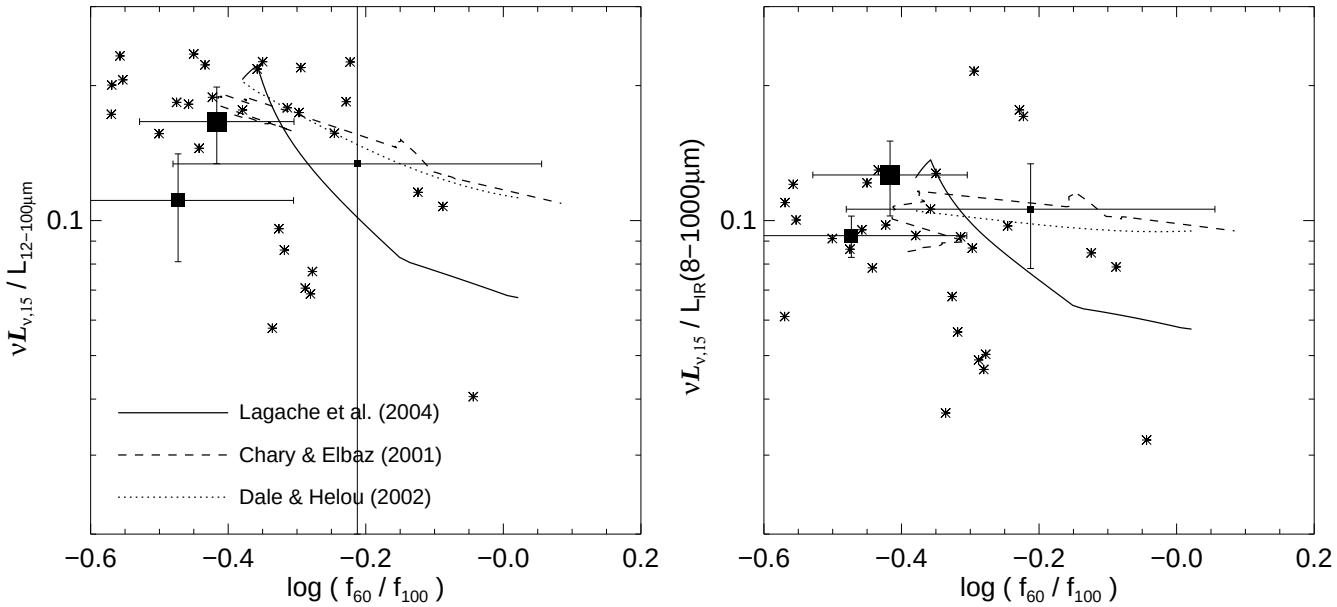

F . 9.— The ratio between the rest-frame 15 μm to the 12–100 μm luminosity (*left* plot) and to the total IR luminosity (8–1000 μm; *right* plot) as a function of the IR flux ratio f_{60}/f_{100}. *Asterisks* are local galaxies collected from literature with IRAS, ISO 15 μm observations and at least one observation at wavelengths longer than 100 μm. *Squares* show our results for galaxies with $M^* \geq 10^{10}\,M_\odot$ and 0.6< z <0.8. The relations derived from SED templates are presented for comparison. One can see that the extrapolation of the rest-frame 15 μm luminosity based on the three sets of templates give comparable estimates of total IR luminosity within a considerable scatter. Our data points distribute within the scatter of the local star-forming galaxies but towards the colder templates. Roughly speaking, a factor of 10 is a quite good average bolometric correction to the estimate of the total IR luminosity from the rest-frame 15 μm luminosity. Generally speaking, the use of local templates of $L_{\rm IR} \leq 10^{10.5}\,L_\odot$ for extrapolation of total IR luminosity from intermediate redshift 24 μm luminosities gives a more accurate result than the use of $L_{\rm IR} \sim 10^{11}\,L_\odot$ templates.

and Dale & Helou (2002). The three sets of templates were empirically calibrated to represent local star-forming galaxies spanning a wide range in the IR flux ratio f_{60}/f_{100}. Dale & Helou's IR SED templates are characterized by the flux ratio f_{60}/f_{100}. We use the equation from Chapman et al. (2003) to parameterize the IR luminosity (8 - 1000 μm) as a function of f_{60}/f_{100}.[8] The templates from Lagache et al. (2004) and Chary & Elbaz (2001) were characterized by the IR luminosity. We extended each set of SED templates by linear interpolation in logarithmic space to a grid of SEDs with the characteristic IR luminosity ranging from 10^9 to $10^{13}\,L_\odot$ with a resolution of 0.1 dex. The observed IR SED of each subset was compared to the three sets of templates:

$$\chi^2 = \sum_{i=1}^{N_{\rm filters}} \left[\frac{L_{{\rm obs},i} - f_{scale} \times L_{{\rm temp},i}(z=0.7)}{\sigma_i} \right]^2 , \qquad (1)$$

where $L_{{\rm obs},i}$, $L_{{\rm temp},i}$ and σ_i are the observed and template luminosities and their uncertainty in filter i, respectively, and $f_{\rm scale}$ is a normalization constant. Here only 24, 70 and 160 μm bands were used to fit templates, i.e., $N_{\rm filters} = 3$. $L_{\rm temp}$ is calculated by convolving the redshifted SED template to $z = 0.7$ with the 24, 70 or 160 μm filter transmission function. $f_{\rm scale}$ is chosen to minimize the χ^2 for each template. The top plot in Figure 8 shows the fitting results. The templates with a normalization constant $f_{\rm scale}$ of unity are chosen as the best-fit luminosity match templates and those with a minimum χ^2 as the best-fit dust temperature match (or SED shape match) templates. The best-fit templates are compared to the observed SEDs in the bottom plot of Figure 8.

As shown in Figure 8 the local SED templates track the observed SEDs reasonably well, in particular for the L_{24}-medium bin, which contains the majority of intense star-forming galaxies. As the total IR luminosity is dominated by emission in the rest-frame wavelength range between 10 and 100 μm, the estimates of the total IR luminosity with templates from different models give similar results. In contrast, χ^2 is a measure of the shape agreement between a template and an observed SED. It is worth noting that the estimate of total IR luminosity based on the three measurements at 24, 70 and 160 μm is not sensitive to the shapes of the IR SED templates. Both the best-fit luminosity match and the best-fit dust temperature match the SED templates and suggest a total IR (8 - 1000 μm) luminosity of $\log L_{\rm IR}/L_\odot \sim 11.4$, 11.1, 10.3 for the three average SEDs, respectively. Generally speaking, the shape (or dust temperature) of the average IR SEDs of star-forming galaxies at $z \sim 0.7$ (i.e., the L_{24}-high bin and L_{24}-medium bin) are better fitted by the local SED templates of characteristic IR luminosity $L_{\rm IR} \leq 10^{11}\,L_\odot$ than those of $L_{\rm IR} > 10^{11}\,L_\odot$. This holds for all three sets of templates. It confirms that the typical star-forming galaxies at $z \sim 0.7$ are likely to have relatively colder dust emission than local galaxies with comparable IR luminosity.

4.4. *The extrapolation from the rest-frame 15 μm to the total IR luminosity*

Local IR SED templates are often used to estimate the total IR luminosities from single mid-IR band luminosities for distant star-forming galaxies. With the averaged IR SEDs determined in the three MIPS bands, we are able to better constrain the estimates of the IR luminosities. We compared the estimates with those transformed from single 15 μm luminosities using local SED templates.

By linearly integrating between the average 24, 70 and 160 μm luminosities (in logarithm space) for the star-forming

[8] The total IR luminosity defined in Chapman et al. (2003) is between 3 and 1100 μm , in good agreement with the adopted one (Dale et al. 2001; see also Takeuchi et al. 2005b).

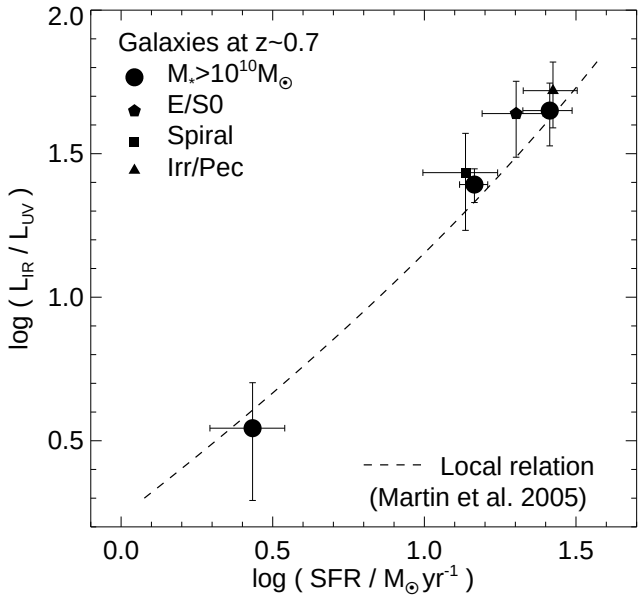

F . 10.— The ratio IR/UV flux (i.e., the fractional dust obscuration) as a function of SFR. *Solid circles* show the three subsets of galaxies with $M_* \geq 10^{10}\,M_\odot$ and $0.6 < z < 0.8$, sorted by the 24 μm luminosity. Other symbols show three morphology subsets of star-forming ($f_{24} > 83\mu$Jy) galaxies in redshift slice $0.65 \leq z \leq 0.75$. The *dashed line* shows the local relation (Martin et al. 2005b).

galaxies at $z \sim 0.7$, we estimated the rest-frame 12–100 μm luminosities. Uncertainties are calculated from the combination of the uncertainties in the three bands. The total IR (the rest-frame 8–1000 μm) luminosity is derived from the three dust temperature-match templates to each observed IR SED (the 24, 70 and 160 μm). We combine the scatter between the templates and the uncertainty in determining the dust temperature-match templates, in which the uncertainties of the 24, 70 and 160 μm luminosities are counted, as the uncertainty for the total IR luminosity. The results are listed in Table 2. For comparison, we use the NASA/IPAC Extragalactic database (NED) to collect a sample of 29 local star-forming galaxies ($z < 0.1$) with observations at 12, 25, 60 and 100 μm by *IRAS*, at 15 μm by ISO and at least in one band longer than 100 μm. The 12–100 μm luminosity and the total IR luminosity are calculated as above. When observations do not reach 1000 μm, a modest ($\lesssim$ 20% of the IR luminosity) extrapolation is employed using the local SED templates.

Figure 9 shows the extrapolations (bolometric corrections) from the rest-frame 15 μm to the 12–100 μm luminosity (left plot) and to the total IR luminosity (right plot) as functions of the IR flux ratio f_{60}/f_{100}. The local star-forming galaxies exhibit a significant scatter (Chary & Elbaz 2001; see also Dale et al. 2005); such scatter is typically adopted as the systematic uncertainty of template-based estimates of total IR luminosity from rest-frame mid-IR luminosity. The $z \sim 0.7$ star-forming galaxies distribute within the scatter of the local star-forming galaxies. Again, there is a tendency for the $z \sim 0.7$ galaxies to cluster towards the colder templates, suggesting that use of spiral galaxy templates for extrapolation of total IR luminosity from intermediate redshift 24 μm fluxes gives a more accurate result than the use of starburst/LIRG templates.

4.5. *Dust extinction*

A universal relation between SFR and dust extinction is suggested by several studies at $z < 1$ (Hopkins et al. 2001; Adelberger & Steidel 2000; Bell 2003; Takeuchi et al. 2005a; Zheng et al. 2006; Buat et al. 2006; although see Reddy et al. 2006 for a dissenting view at $z \sim 2$). With a measured estimate of the total IR luminosity from the 24, 70 and 160 μm luminosities, we explore the relationship between SFR and dust extinction at $z \sim 0.7$, comparing it to that at $z \sim 0$. The dust extinction is described by the IR to UV ratio $L_{\rm IR}/L_{\rm UV}$. The UV luminosity, i.e., the integrated luminosity between rest-frame 1500-2800 Å, is estimated from linear interpolation of the *FUV*, *NUV*, *U*, and *B* band luminosities for $z \sim 0.7$ galaxy subsets shown in Figures 5 and 6. Following Bell et al. (2005), we derived the SFR from the IR and UV luminosities with the formula

$$\mathrm{SFR}/(M_\odot\,\mathrm{yr}^{-1}) = 9.8\times10^{-11}(L_{\rm IR} + 2.2L_{\rm UV}), \qquad (2)$$

assuming a stellar population with a constant SFR for 100 Myr and a Kroupa initial mass function. Figure 10 shows the relationship between dust obscuration and SFR for $z \sim 0.7$ galaxies, compared to the local relation derived from IRAS and GALEX data with a scatter at ~0.5-1 dex level (Martin et al. 2005b; Xu et al. 2006; Buat et al. 2006). As shown in Figure 10, the $z \sim 0.7$ galaxies distribute perfectly along the local relation over one order of magnitude.

5. DISCUSSION AND CONCLUSION

We selected a sample of 152 galaxies in the redshift slice $0.65 \leq z \leq 0.75$ of known morphology from HST imaging and another sample of 579 mass-limited ($M_* \geq 10^{10}\,M_\odot$) galaxies in the redshift slice $0.6 < z < 0.8$ to study the IR SEDs at that redshift. We divided our sample galaxies into different mass-limited morphology and 24 μm luminosity bins. For each bin, we determined the average luminosities in 14 bands from the FUV to the FIR by summing the individual detections and adding in the stacked flux from non-detections. Careful efforts were taken in stacking the noise and confusion limited 70 and 160 μm images. Empirical corrections, determined from the 24 μm image, were introduced to account for the clustering effects on the stack results.

The average luminosities in three MIPS bands determine the IR SED from the rest-frame 10 to 100 μm. Our principal result is that the average IR SED shape of $z \sim 0.7$ intensely star-forming galaxies (with IR luminosities $\sim 10^{11}L_\odot$) is similar to reasonably 'cool' local templates (i.e., templates of 'normal' spiral galaxies). The dust SED seems to depend on morphological type for star-forming galaxies at $z \sim 0.7$. This has the immediate and important implication that the use of local templates to extrapolate total IR luminosity from observed-frame 24 μm data is a well-posed problem, at least, on average. Interestingly, galaxies with 'cool' dust temperatures in the local Universe all tend to have IR luminosities $\lesssim 10^{10.5}L_\odot$, i.e., distant intensely star-forming galaxies tend to be characterized by colder dust emission than their local counterparts of comparable IR luminosity.

Previous studies have found evidence for a somewhat cooler dust SED at $0.2 < z < 2.5$ than for local galaxies of a comparable luminosity (e.g., Pope et al. 2006; Sajina et al. 2006) at $0.2 < z < 2.5$. These studies were selected in rest-frame > 100 μm emission, and the authors suspected that their overall tendency towards 'colder' IR SEDs was in part due to that long-wavelength selection. Our sample is selected on rest-frame $\sim$ 15 μm emission, i.e., by warm dust; yet, we find a 'colder' average SED at a given luminosity than is found locally. This tends to support the interpretation that the offset which we and others have found towards colder temperatures at a given luminosity are at least in part a real difference.

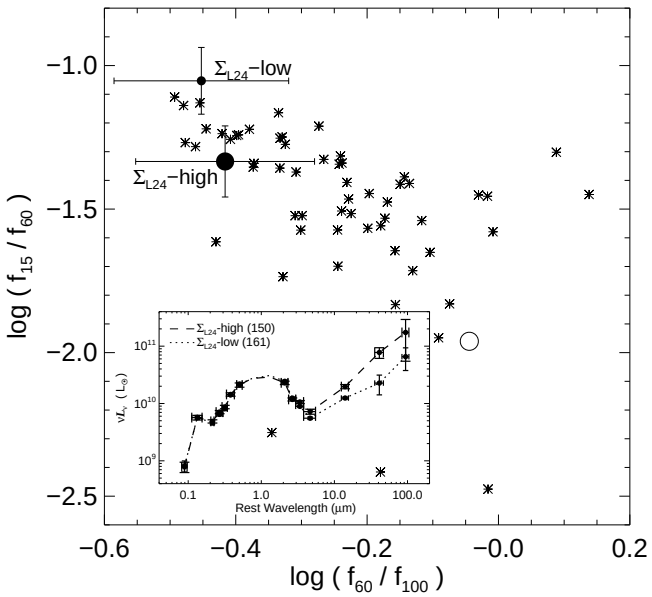

F . 11.— Same as Fig. 7. The *filled circles* show the two subsets of galaxies in the redshift slice $0.6 < z < 0.8$ split by 24 μm luminosity surface density. The inner panel shows the average SEDs of the two subsets. The Σ_{L24}-high bin and the Σ_{L24}-low bin data points are located separated along the dust-temperature sequence of local star-forming galaxies, indicating that the Σ_{L24}-high bin is characterized by a hotter dust emission than the Σ_{L24}-low bin. This is clearly seen from the difference between their IR SEDs.

We suggest that this tendency toward colder dust temperature reflects a difference in dust and star formation geometry: whereas local LIRGs tend to be interacting systems with relatively compact very intense star formation and of comparable masses (e.g., Wang et al. 2006), $0.5 \lesssim z \lesssim 1$ LIRGs tend to be disk-dominated, relatively undisturbed galaxies (Zheng et al. 2004; Bell et al. 2005; Melbourne et al. 2005). We suggest that these disk galaxies host widespread intense star formation, like star formation in local spirals but scaled up, leading to relatively cold dust temperatures. This is consistent with what Chanial et al. (2006) found — the scatter in the $L_{\rm IR} - T_{\rm dust}$ relation for star-forming galaxies is largely induced by the size dispersion of the star-forming regions; and the IR luminosity surface density $\Sigma_{\rm IR} - T_{\rm dust}$ relation is more fundamental than the the $L_{\rm IR} - T_{\rm dust}$ relation. We examined the IR flux ratio f_{60}/f_{100} (indicator of dust temperature) as a function of the IR luminosity surface density for $z \sim 0.7$ star-forming galaxies. By taking galaxy size (i.e. half-light radius) derived from HST imaging (Häußler et al. 2007) as a proxy of the size of star-forming regions in a galaxy and 24 μm luminosity as a proxy of total IR luminosity, we split a sample of 311 24 μm-detected galaxies in the redshift slice $0.6 < z < 0.8$ into two bins in the 24-μm luminosity surface density Σ_{L24}. The average SEDs for the two subsets of galaxies were constructed in the same way as described in §4.1 and shown in the inner panel of Figure 11. The total IR luminosity is estimated as $\log(L_{\rm IR}/L_\odot) = 11.3$ and 11.0 for the Σ_{L24}-high bin and the Σ_{L24}-low bin respectively. As shown in Figure 11, the two subpopulations are distributed along the dust-temperature sequence of local star-forming galaxies. Galaxies in the Σ_{L24}-high bin on average show hotter dust emission than those in the Σ_{L24}-low bin, suggesting that the IR luminosity surface density plays an essential role in shaping IR SED (Chanial et al. 2006).

Finally, with UV luminosities derived from GALEX data and IR luminosities derived from three band MIPS data, we determined a quite precise relationship between the dust obscuration and SFR for z ~0.7. Our results show an excellent agreement between the SFR-dust obscuration relation at z ~0.7 with that at the present day, indicating that no significant evolution occurs since that redshift. Our measurements give the mean values of SFR and dust obscuration. The actual scatter in dust obscuration can spread by 1 - 2 dex for individual galaxies of given SFR(Martin et al. 2005b; Xu et al. 2006; Buat et al. 2006). Reddy et al. (2006) claimed that the dust obscuration for star-forming galaxies is systematically smaller at $z \sim 2$ than the present day. Their sample is dominated by rest-frame UV-selected galaxies. This may lead to a potential selection bias against objects with high IR/UV ratio (see Buat et al. 2006 for the comparison between UV and FIR selected samples of local galaxies and a similar discussion). Therefore studies based on unbiased samples of high-redshift galaxies will help to answer the question whether the SFR-dust obscuration relation still holds at $z > 1$. This will add important constraints to our understanding of galaxy evolution involving star formation and metallicity enrichment (Zheng et al. 2006).

We are grateful to Daniel A. Dale and Kirsten K. Knudsen for helpful discussions. E. F. B. was supported by the Emmy Noether Programme of the Deutsche Forschungsgemeinschaft. Support for E. L. F.'s work was provided by NASA through the Spitzer Space Telescope Fellowship Program. This work was in part supported by contract 1255094 from JPL/Caltech to the University of Arizona. This research has made use of the NASA/IPAC Extragalactic Database (NED) which is operated by the Jet Propulsion Laboratory, California Institute of Technology, under contract with the National Aeronautics and Space Administration.

REFERENCES

Adelberger, K. L., & Steidel, C. C. 2000, ApJ, 544, 218
Appleton, P. N., et al. 2004, ApJS, 154, 147
Bell, E. F. 2003, ApJ, 586, 794
Bell, E. F., et al. 2005, ApJ, 625, 23
Borch, A., et al. 2006, A&A, 453, 869
Borys, C., et al. 2006, ApJ, 636, 134
Brand, K., et al. 2006, ApJ, 644, 143
Buat, V., et al. 2006, ApJS, in press (astro-ph/0609738)
Chanial, P., Flores, H., Guiderdoni, B., Elbaz, D., Hammer, F., & Vigroux, L. 2006, A&A in press (astro-ph/0610900)
Chapman, S. C., Helou, G., Lewis, G. F., & Dale, D. A. 2003, ApJ, 588, 186
Chary, R., & Elbaz, D. 2001, ApJ, 556, 562
Dale, D. A., et al. 2000, AJ, 120, 583
Dale, D. A., & Helou, G. 2002, ApJ, 576, 159
Dale, D. A., Helou, G., Contursi, A., Silbermann, N. A., & Kolhatkar, S. 2001, ApJ, 549, 215
Dale, D. A., et al. 2005, ApJ, 633, 857
Diolaiti, E., Bendinelli, O., Bonaccini, D., Close, L., Currie, D., & Parmeggiani, G. 2000, A&AS, 147, 335
Dole, H., et al. 2004a, ApJS, 154, 87
Dole, H., et al. 2004b, ApJS, 154, 93
Dole, H., et al. 2006, A&A, 451, 417
Elbaz, D., et al. 2002, A&A, 384, 848
Fazio, G. G., et al. 2004, ApJS, 154, 10
Flores, H., et al. 1999, ApJ, 517, 148
Flores, H., et al. 2004, A&A, 415, 885
Frayer, D. T., et al. 2006, AJ, 131, 250
Hammer, F., Flores, H., Elbaz, D., Zheng, X. Z., Liang, Y. C., Cesarsky, C 2005, A&A, 430, 115
Hauser, M. G., & Dwek, E. 2001, ARA&A, 39, 249
Häußler, B., et al. 2007, ApJ, submitted

Hopkins, A. M., Connolly, A. J., Haarsma, D. B., & Cram, L. E. 2001, AJ, 122, 288
Huang, J.-S., et al. 2004, ApJS, 154, 44
Kauffmann, G., et al. 2003, MNRAS, 341, 54
Lagache, G., Dole, H., & Puget, J.-L. 2003, MNRAS, 338, 555
Lagache, G., et al. 2004, ApJS, 154, 112
Lagache, G., Puget, J.-L., & Dole, H., 2005, ARA&A, 43, 727
Le Fèvre, O., et al. 2005, A&A, 439, 845
Le Floc'h, E., et al. 2005, ApJ, 32, 169
Lehmer, B. D., et al. 2005, ApJS, 161, 21
Marcillac, D., Elbaz, D., Chary, R. R., Dickinson, M., Galliano, F., & Morrison, G. 2006, A&A, 451, 57
Martin, D. C., et al. 2005a, ApJ, 619, L1
Martin, D. C., et al. 2005b, ApJ, 619, L59
Melbourne, J., Koo, D. C., & Le Floc'h, E. 2005, ApJ, 632, L65
Morrissey, P., et al. 2005, ApJ, 619, L7
Papovich, C., & Bell, E. F. 2002, ApJ, 579, L1
Papovich, C., et al. 2004, AppJS, 152, 163
Pope, A., et al. 2006, MNRAS, 370, 1185
Pozzi, F., et al. 2004, ApJ, 609, 122
Reddy et al. 2006, ApJ, 644, 792
Rieke, G. H., et al. 2004, ApJS, 154, 25
Rix, H.-W., et al. 2004, ApJS, 152, 163
Sajina, A., Scott, D., Dennefeld, M., Dole, H., Lacy, M. & Lagache, G. 2006, MNRAS, (astro-ph/0603614)
Soifer, B. T., & Neugebauer, G. 1991, AJ, 101, 354
Takeuchi, T. T., Buat, V., & Burgarella, D. 2005a, A&A, 440, L17
Takeuchi, T. T., Buat, V., Iglesias-Páramo, J., Boselli, A., & Burgarella, D. 2005b, A&A, 432, 423
Vanzella, E., et al. 2005, A&A, 434, 53
Vanzella, E., et al. 2006, A&A, 454, 423
Wang, J. L., Xia, X. Y., Mao, S. D., Cao, S., Wu, H., & Deng, Z. G. 2006, ApJ, 649, 722
Wolf, C., Meisenheimer, K., Rix, H.-W., Borch, A., Dye, S., & Kleinheinrich, M. 2003, A&A, 401, 73
Wolf, C., et al. 2004, A&A, 421, 913
Xu, K. C., Lonsdale, C. J., Shupe, d. L., Franceschini, A., Martin, C., & Schiminovich, D. 2003, ApJ,587, 90
Xu, K. C., et al. 2005, ApJ, 619, L11
Xu, K. C., et al. 2006, ApJ, 646, 834
Yan, L., et al. 2005, ApJ, 628, 604
Zheng, X. Z., et al. 2006, ApJ, 640, 784
Zheng, X. Z., Hammer, F., Flores, H., Assémat, F., & Pelat, D. 2004, A&A, 421, 847